Metal−Organic Framework Decorated Polymer Nanofiber Composite Separator for Physiochemically Shielding Polysulfides in Stable Lithium−Sulfur Batteries

Shujun Zheng, Xiaobo Zhu, Yue Ouyang, Kai Chen, Ai-Long Chen, Xiaoshan Fan, Yue-E Miao,* Tianxi Liu, and Yi Xie*

Cite This: *Energy Fuels* 2021, 35, 19154−19163

Read Online

ACCESS | Metrics & More | Article Recommendations | Supporting Information

ABSTRACT: Lithium−sulfur (Li−S) batteries have attracted numerous attention owing to their overwhelming theoretical capacity. However, the dissolution and shuttle effect of lithium polysulfides (LiPSs) have seriously limited the development of Li−S batteries. Herein, we rationally designed a dual-engineered nanofibrous composite separator with a Janus structure to both physically and chemically block LiPS shuttling in Li−S batteries. The separator, consisting of a cross-linked poly(vinyl alcohol)/poly(acrylic acid) (CPP) composite nanofiber matrix and the electrosprayed poly(vinyl alcohol) (PVA)/zeolitic imidazolate framework-8 (ZIF-8) layer on the cathode side, is fabricated through a facile electrospinning−electrospray coupling approach and signed as CPP@PVA/ZIF-8. The intrinsic narrow size and opened Lewis acid sites of ZIF-8 both confine free transport of LiPS anions. Meanwhile, the cross-linked CPP layer with abundant electronegative groups (−COOH) can shield the LiPS shuttle while ensuring the integrity of the flexible separator. Benefiting from the unique Janus structure, the CPP@PVA/ZIF-8 separator demonstrates a high initial capacity of 1125 mAh g^{-1} at a good coulombic efficiency of 98% over 300 cycles at 0.1 C. This work not only establishes a combined strategy to immobilize LiPSs but also provides novel interfacial engineering modification ideas for the development of high-performance separators in Li−S batteries.
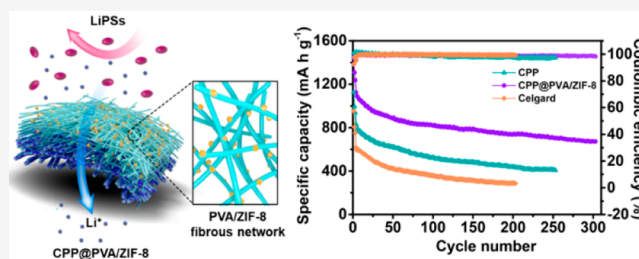
1. INTRODUCTION

Lithium−sulfur (Li−S) batteries are considered as one kind of the most promising high-energy storage systems for their high theoretical capacity (1675 mAh g^{-1}) and high energy density (2600 Wh kg^{-1}) by combining with the naturally abundant sulfur cathode and metallic lithium anode with the lowest potential (−3.04 V versus standard hydrogen electrode).[1−4] However, there are several intricate issues limiting the practical application of Li−S batteries: (i) the large volumetric variation of the sulfur cathode,[5,6] (ii) the dendritic growth of the Li metal anode,[7] and (iii) the shuttle effect between insulate sulfur and lithium sulfides.[8,9] Among these challenges, the repeating shuttle of soluble lithium polysulfides [LiPSs, i.e., Li$_2$S$_n$ (4 < n < 8)] is regarded as the fatal obstacle. During the charge/discharge process, LiPSs generated from the solid−liquid−solid multiphase conversions are easily dissolved in the liquid electrolyte and migrate across the separator, thus leading to the corrosion of the lithium anode.[10−12] As a result, a series of troubles would be induced in the working battery, including low coulombic efficiency, irreversible loss of active material, and fast capacity fading. Therefore, developing effective regulation strategies to suppress the shuttle effect of LiPSs is of great significance for high-performance Li−S batteries.

Following this direction, extensive designs of advanced porous hosts, such as graphite oxide,[13] metal oxides,[14,15] and porous hollow carbon materials,[16,17] have been integrated into the sulfur cathode to address the dissolved LiPSs through physicochemical adsorptions. Nonetheless, such modifications on the cathode side will inevitably introduce additional agents and reduce the sulfur content, thus sacrificing the overall energy density of Li−S batteries.[18] Furthermore, the weak affinity toward LiPS intermediates can hardly prevent the migration of LiPSs completely during the repeated cycles. As a necessary component in the batteries, the commercial separator based on polyethylene (PE) or polypropylene (PP) plays the key role in preventing the electrical contact between the cathode and anode as well as enabling the lithium ion diffusion.[19−21] However, the commercial separator cannot block the transport of soluble LiPSs as a result of the missing of

polar active sites. Besides, these polyolefin separators display poor electrochemical performance in electrolyte wettability, mechanical property, and thermal stability.[22] Therefore, very recent studies have been focused on the modification of PP separators to suppress LiPS shuttling and achieve the long life of Li−S batteries.[23] Various materials, such as conducting polymers,[24,25] N-doped graphene,[26,27] Prussian blue analogues,[28] and metal−organic frameworks (MOFs),[29−32] have been assembled on the surface of the PP separator. The migration of intermediate polysulfides was significantly restrained, and the longevity of the Li−S battery could be improved to some degree as a result of the physical confinement and/or chemisorption that originated from the coating layer of the PP separator, as mentioned above. Nonetheless, the dense building blocks in the separator inevitably deteriorate the electrolyte wettability. Even worse, the sluggish lithium ion conduction kinetics could hardly meet the necessary electrochemical performance under high rates. To this end, it is highly desirable to develop high-performance separators with both satisfactory reaction kinetics and efficient LiPS interception for Li−S batteries.

MOF-based composite membranes integrating MOFs with functional polymer matrixes hold great promise in the practical application of Li−S separators.[33,34] MOFs, constructed by metal ions and organic ligands, possess abundant Lewis acid sites and highly ordered pores with tunable porosity for potentially suppressing the shuttling of LiPSs in Li−S batteries.[35] Similarly, polymer materials with electronegative groups like −SO₃⁻ and −COOH also demonstrated the electrostatic repulsion of polysulfide anions.[36−38] Herein, we designed a novel dual-engineered MOF-decorated polymer nanofiber separator with a Janus structure through a facile electrospinning−electrospray coupling approach. The composite separator consisting of a cross-linked poly(vinyl alcohol)/poly(acrylic acid) (CPP) composite nanofiber membrane asymmetrically decorated with zeolitic imidazolate framework-8 (ZIF-8) nanoparticles is referred to as CPP@PVA/ZIF-8. The mechanically cross-linked CPP nanofiber layer contains abundant −COOH groups, which enables the efficient electrostatic repulsion to negatively charged LiPSs. Meanwhile, the Lewis acid Zn sites and narrow aperture size of ZIF-8 particles could effectively suppress the shuttle effect of LiPS anions through the physicochemical adsorption interactions. Consequently, the integrated CPP@PVA/ZIF-8 nanofiber separator with high porosity can both allow for the fast ion transport and inhibit the LiPS shuttling synergistically to achieve long-term cyclability and ultraslow capacity decay of the Li−S battery, even at high rates.

2. EXPERIMENTAL SECTION

2.1. Materials. Poly(vinyl alcohol) (PVA; M_w = 89 000−98 000) and poly(acrylic acid) (PAA; M_w = 450 000) were obtained from Sigma-Aldrich Co., Ltd. Zinc nitrate hexahydrate [Zn(NO₃)₂·6H₂O] and methanol were purchased from Sinopharm Chemical Reagent Co., Ltd. 2-Methylimidazole was provided by Sigma-Aldrich Co., Ltd. All of the chemicals were used without further purification.

2.2. Preparation of the CPP Composite Nanofiber Membrane. The polymer nanofiber membranes were prepared by a typical electrospinning process.[39,40] For the preparation of PVA/PAA precursor solution, 5 wt % PVA solution was prepared by stirring PVA powder in ultrapure water at 95 °C for 5 h. Then, PAA at a mass loading of 5 wt % was mixed with the above PVA aqueous solution under continuous stirring for 24 h at room temperature. The electrospinning of the PVA/PAA nanofiber membrane was carried out

in a 5 mL syringe pump at a feeding rate of 0.08 mm min⁻¹ with a high voltage of 18 kV. The distance between the needle tip and collector was set as 15 cm. Meanwhile, the electrospinning condition was fixed at an ambient temperature of 25 °C and air humidity of 35 ± 3%. After that, the PVA/PAA composite nanofiber membrane was treated in the vacuum oven at 120 °C for 3 h, to obtain the CPP composite membrane.

2.3. Preparation of the CPP@PVA/ZIF-8 Composite Separator. Typically, 1.68 g of Zn(NO₃)₂·6H₂O and 3.7 g of 2-methylimidazole were separately dissolved in 80 mL of methanol at room temperature. Then, the Zn(NO₃)₂·6H₂O solution was added to the 2-methylimidazole solution under constant stirring for 24 h at 25 °C. The collected sediments were washed with methanol several times and dried in a vacuum. Thus, ZIF-8 nanoparticles were obtained.

Then, the PVA/ZIF-8 solution was prepared by dispersing 0.2 g of ZIF-8 particles in 10 mL of 5 wt % PVA aqueous solution with vigorous stirring for 12 h. Using a high-voltage electrospraying method, the PVA/ZIF-8 dispersion solution was selectively sprayed on one side of the PVA/PAA composite membrane at a voltage of 30 kV. After that, the PVA/PAA@PVA/ZIF-8 membrane was treated at the same condition as the PVA/PAA membrane to obtain the CPP@PVA/ZIF-8 composite separator.

2.4. Characterization. The morphologies of various separators were observed by scanning electron microscopy (SEM, Hitachi S-4800). X-ray diffraction (XRD) patterns were measured on a Rigaku Dmax 2500 using Cu Kα radiation. Transmission electron microscopy (TEM) images were collected from JEM-2100F (JEOL, Japan). The tensile strength and tensile modulus were tested by a universal testing machine (AG-5000G, Shimadzu, Japan) with a tensile speed of 5 mm min⁻¹ at room temperature. Contact angles were conducted on a Dataphysics OCA40 Micro machine. Thermogravimetric analysis (TGA) was performed under an oxygen atmosphere with a Q5000IR analyzer. Fourier transform infrared spectroscopy (FTIR, Nicolet iN10 MX/Nicolet 6700) was taken using an attenuated total reflection (ATR) mode. X-ray photoelectron spectroscopy (XPS) was conducted using a VG ESCALAB 220i-XL system. Nitrogen adsorption/desorption measurements were performed by a Quadrasorb adsorption instrument. The specific surface area was calculated using the multi-point Brunauer−Emmett−Teller (BET) test. According to the nitrogen adsorption data and non-local density functional theory (NLDFT) equilibrium model, the pore size distribution was analyzed using the Quantachrome data software (ASIQwin, version 4.01).

The porosity of the membrane was measured by a liquid absorption method and calculated according to the following equation:[20]

$$\text{porosity} = \frac{W_w - W_0}{\rho_1 V} \tag{1}$$

The density of the membrane was calculated by the following equation:

$$\text{density } (\rho) = \frac{W_0}{V} \tag{2}$$

where W_0 is the original weight of the separator, W_w is the weight of separator immersed in 1,3-dioxolane (DOL) for 1 h, and ρ_1 and V represent the density of DOL and the volume of the separator, respectively.

The electrolyte uptake (U) and retention (R) of the separator was also acquired on the basis of the following equations:[41]

$$R = \frac{W_X - W_0}{W_1 - W_0} \times 100\% \tag{3}$$

$$U = \frac{W_1 - W_0}{W_0} \times 100\% \tag{4}$$

W_0 and W_1 are the original weight of the separator and the weight after soaking in the electrolyte for 1 h, respectively. After that, the separator stood at 50 °C in an oven and its equilibrium weight (W_X) was measured at various times.
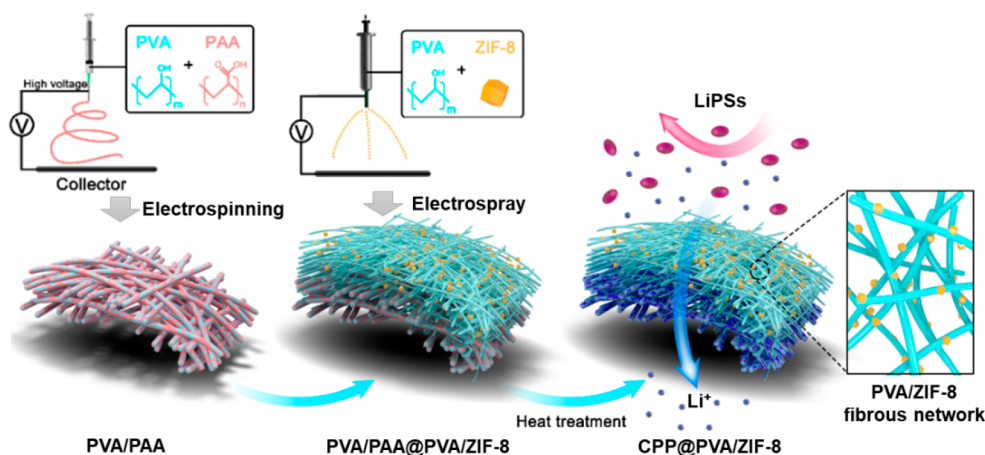
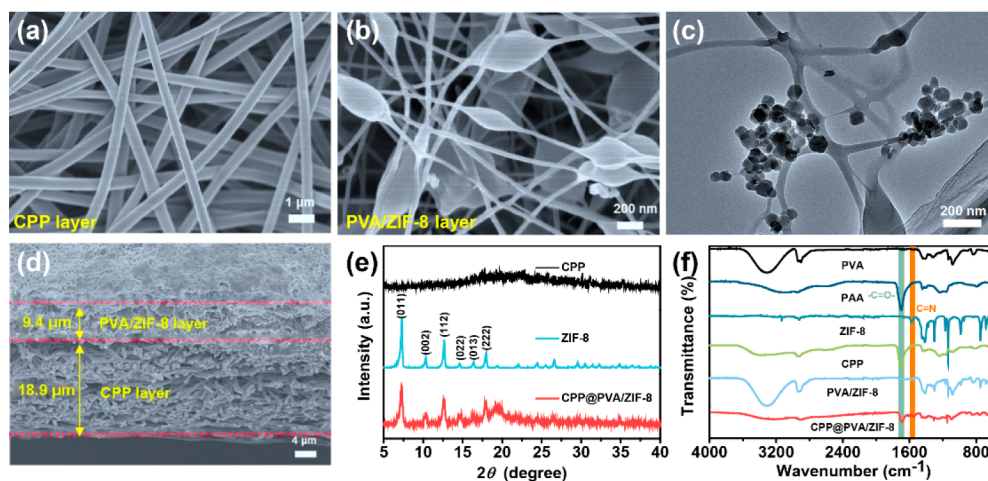**Figure 1.** Schematic illustration showing the preparation of the CPP@PVA/ZIF-8 composite separator.

Figure 2. Surface morphologies of the CPP@PVA/ZIF-8 separator along the (a) CPP layer side and (b) PVA/ZIF-8 layer side, (c) TEM image of the PVA/ZIF-8 layer, (d) cross-sectional image of the CPP@PVA/ZIF-8 separator, and (e) XRD patterns and (f) FTIR spectra of different samples.

2.5. Electrochemical Measurements. Sulfur cathodes were prepared by mixing 6 wt % active material, 3 wt % carbon black, and 1 wt % poly(vinylidene fluoride) (PVDF) binder in N-methylpyrrolidone (NMP) solution, which was then cast onto aluminum foil. The average sulfur loading was fixed at 1.2 mg cm^{-2} if not specifically mentioned. The CR2032 standard cells were assembled in an argon-filled glovebox using sulfur as the cathode, lithium metal as the anode, and various samples as separators. Typically, 35 μL of liquid electrolyte containing 1.0 M bis(trifluoromethane)sulfonimide lithium (LiTFSI) mixing with DOL/dimethoxyethane (DME) (1:1, v/v) and 1 wt % lithium nitrate (LiNO$_3$) was used without further purification. Thus, the electrolyte volume to active sulfur mass ratio, generally presented as E/S, was 25.8 μL mg^{-1} in this work. The charge–discharge tests were conducted using the NEWARE instrument with a given voltage window of 1.7–2.8 V. Electrochemical impedance spectroscopy (EIS) was performed on a CHI660E electrochemical workstation with a potential range of 1.7–2.8 V and frequency of 0.1–10^5 Hz, while cyclic voltammetry (CV) measurements were obtained at the scanning rate of 0.5 mV s^{-1}.

Each separator was separately assembled between two stainless-steel electrodes in a coin-type battery. Thus, the ionic conductivity was determined by the following equation:

$$\sigma = \frac{L}{RA} \qquad (5)$$

where σ is the ionic conductivity, R is the bulk resistance, and L and A represent the thickness and area of the separator, respectively.

The Li$^+$ transference number (t_{Li^+}) was measured with chronoamperometry using a Li|Li symmetric cell (CR2032) at a constant step potential of 10 mV. The specific values were calculated according to the following equation:

$$t_{Li^+} = \frac{I_S}{I_0} \qquad (6)$$

where I_S and I_0 represent the steady-state and initial-state currents, respectively.

The lithium ion diffusion coefficients in various membranes were calculated through two methods. In the first method, the diffusion coefficient of the lithium ion was calculated on the basis of EIS results according to the following equations:[42]

$$D_{Li^+} = \frac{R^2 T^2}{0.5 A^2 n^4 F^4 C^2 \sigma^2} \qquad (7)$$

$$Z = R_e + R_{ct} + \sigma \omega^{-0.5} \qquad (8)$$

where n is the number of electrons in the oxidation reaction of each molecule, A is the surface area of the positive electrode, D_{Li^+} is the diffusion coefficient of Li$^+$, R is the gas constant, T is the absolute temperature, F is the Faraday constant, C is the concentration of Li$^+$, and σ is the slope of the approximate linear distribution between Z'
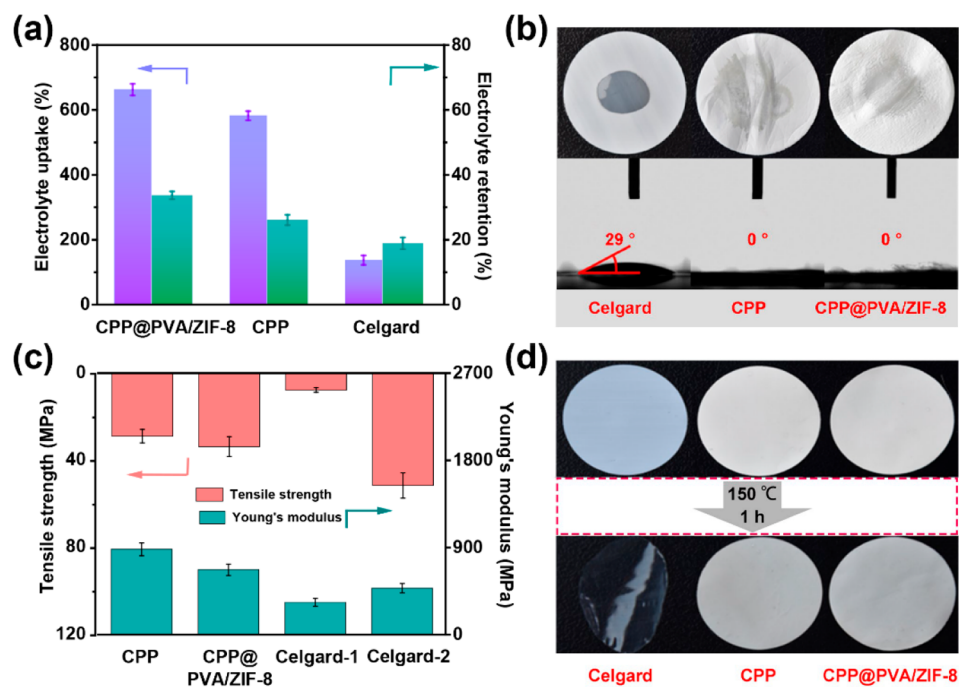
Figure 3. Physical properties of different separators: (a) electrolyte uptake and retention, (b) contact angle measurements with the electrolyte, (c) mechanical properties, and (d) optical pictures before and after thermal treatment.

and the square root of the frequency ($\omega^{0.5}$) in the low-frequency region.

The second method to calculate the lithium-ion diffusion coefficients of Celgard, CPP, and CPP@PVA/ZIF-8 in different reaction stages was conducted through a series of CV measurements with different scanning rates. The peak current was then analyzed using the Randles–Sevcik equation:[43]

$$I_p = 2.69 \times 10^5 n^{1.5} A D_{Li^+}^{0.5} C_{Li} \nu^{0.5} \qquad (9)$$

where I_p represents the peak current (A), n stands for the number of electrons involved in the reaction (Li–S battery; $n = 2$), A is the electrode area (cm^2), C_{Li} refers to the Li$^+$ concentration (mol L^{-1}), and ν is the scanning rate (V s^{-1}).

3. RESULTS AND DISCUSSION

Figure 1 illustrates the preparation process of the multifunctional CPP@PVA/ZIF-8 composite separator, which involves the electrospinning and electrospray procedures. In the first step, the PVA/PAA nanofiber membrane is fabricated by a simple and efficient electrospinning technique. Then, the flexible CPP@PVA/ZIF-8 membrane is achieved by directly spraying PVA/ZIF-8 solution on one side of the previously collected PVA/PAA nanofiber membrane. After thermal treatment, the hydroxyl group (−OH) in PVA and the carboxyl group (−COOH) in PAA are cross-linked to obtain the CPP@PVA/ZIF-8 composite separator with greatly increased mechanical properties and chemical stability. Morphology of the CPP membrane shows randomly distributed nanofibers with a diameter around 400 nm in Figure 2a, which indicates no obvious difference from the PVA/PAA composite nanofibers (Figure S1a of the Supporting Information). On the basis of the fact that electrical charges would repel each other in the electrospray process, the electrosprayed PVA/ZIF-8 layer with good self-dispersive properties can easily penetrate into the PVA/PAA nanofiber network, thus resulting in an integrated Janus network after the

thermal cross-linking of the whole separator. Additionally, the efficient combination of PVA and ZIF-8 is expected to form a three-dimensional (3D) LiPS barrier, which can exert the polysulfide trapping effect of ZIF-8. In comparison to the smooth surface of the CPP composite membrane (panels b and c of Figure S1 of the Supporting Information), the PVA/ZIF-8 layer presents a spindle-like PVA network firmly anchored with abundant polyhedral-like ZIF-8 nanoparticles (panels b and c of Figure 2 and Figure S2 of the Supporting Information). The high porosity in both the CPP and PVA/ZIF-8 layers can guarantee the electrolyte wettability and facilitate rapid Li$^+$ transfer, thus largely improving the ionic conductivity. Benefiting from the thermal cross-linking reaction, the cross-section of the CPP@PVA/ZIF-8 separator indicates a perfect Janus structure (Figure 2d), where the supporting CPP layer with a thickness of 18.9 μm has close contact with the functional PVA/ZIF-8 layer in a thickness of 9.4 μm.

XRD patterns of both CPP and CPP@PVA/ZIF-8 display a wide peak at about $2\theta = 20°$ (Figure 2e), which is attributed to the (101) reflection of PVA.[38] The peaks at $2\theta = 7.3°$, 10.4°, 12.7°, 14.7°, 16.4°, and 18.0°, corresponding to the (011), (002), (112), (022), (013), and (222) crystal surfaces of ZIF-8,[44−46] respectively, indicate the successful synthesis and incorporation of ZIF-8 nanoparticles in the CPP@PVA/ZIF-8 composite membrane. FTIR is further conducted to verify the chemical structure of the CPP@PVA/ZIF-8 composite membrane (Figure 2f). The characteristic peak at 3000–3700 cm^{-1} is caused by the bending vibration of the −OH group in PVA, while the peaks at 1704 and 2800–3700 cm^{-1} are assigned as the stretching vibration of the carbonyl group (−C=O−) and the hydrogen-bond interactions between −COOH groups in PAA, respectively. After thermal treatment, the intensity of the −OH group at 3000–3700 cm^{-1} decreases dramatically, while the −C=O− band is red-shifted to 1714
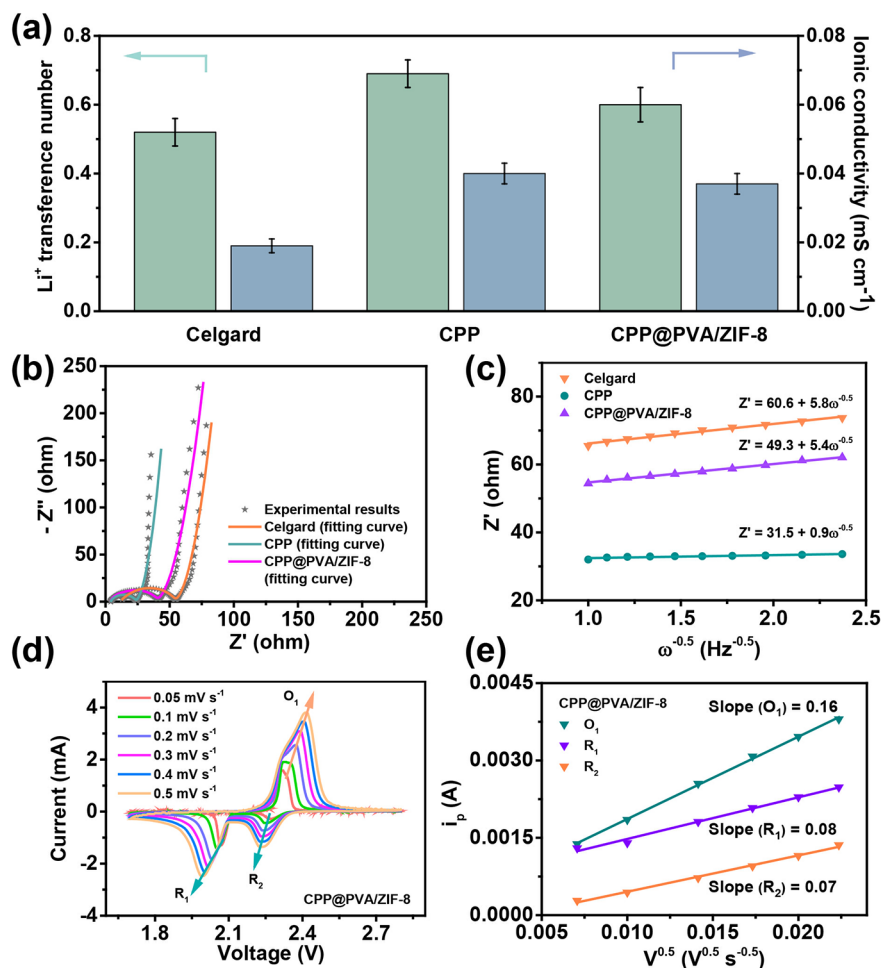
Figure 4. Electrochemical performance of the Li−S batteries with different nanofiber separators: (a) calculated ionic conductivity and Li^{+} transference number, (b) EIS curves and (c) corresponding relationships between Z' and $\omega^{-0.5}$ at the low-frequency region, and (d) CV curves under different scanning rates and (e) corresponding linear fits of the peak currents of CPP@PVA/ZIF-8 separator.

cm[−1], which demonstrates the successful esterification cross-linking reaction between PVA and PAA.[47,48] Furthermore, the characteristic peaks of PVA and ZIF-8 also appear in the CPP@PVA/ZIF-8 membrane. The bending vibrations of C−N and −CH$_2$ on the imidazole ring located at 3136 and 2927.5 cm^{−1} might be concealed by the strong adsorption of −OH in PVA, while the band at 1584 cm^{−1} could be assigned to the tensile vibration of C=N on the imidazole ring in ZIF-8.[44] The FTIR results combined with XRD patterns could provide strong evidence for the efficient loading of ZIF-8 particles in the mechanically cross-linked CPP@PVA/ZIF-8 composite membrane. The corresponding loading content of ZIF-8 in the CPP@PVA/ZIF-8 separator is determined by TGA curves to reach 15.6 wt % (Figure S3 of the Supporting Information).

As is well-known, the ability to capture the liquid electrolyte is essential for the ionic conductivity of separators. As a result of the high surface area of ZIF-8 (1256.9 m[2] g^{−1}; Figure S4 of the Supporting Information) and interconnected fibrous pathways, the CPP@PVA/ZIF-8 composite separator achieves a superior electrolyte adsorption rate (662.4%) and retention rate (33.7%) after heating at 50 °C for 500 min, which are much higher than those of the CPP nanofiber and Celgard separators (Figure 3a and Figure S5 of the Supporting Information). Remarkably, both CPP and CPP@PVA/ZIF-8 separators can immediately adsorb the electrolyte with contact

angles of 0°, whereas a drop of electrolyte remains on the surface of Celgard with a high contact angle of 29°, as demonstrated in Figure 3b. This sharp contrast is mainly due to the hydrophobic nature of the commercial polyolefin separator and intrinsic high porosity (92.1%) of the electrospun nanofiber separators (Table S1 of the Supporting Information). Benefiting from the stable chemical cross-linking between PVA and PAA as well as the good compatibility between CPP and PVA/ZIF-8 layers, the CPP@PVA/ZIF-8 separator also presents robust mechanical properties with a high tensile strength of 33.4 MPa and a Young's modulus of 669 MPa (Figure 3c and Figure S6 of the Supporting Information), which can maintain its structural integrity and effectively prevent short-circuit of the batteries during operation. Conversely, the Celgard separator has obvious anisotropic mechanical properties, only with a low tensile strength of 7.4 MPa and a Young's modulus of 333.3 MPa in the weak direction, being much lower than those of the CPP@PVA/ZIF-8 separator (Table S2 of the Supporting Information). Thermal stability is also a key factor to ensure the battery safety. As shown in Figure 3d, CPP and CPP@PVA/ZIF-8 separators exhibit almost no shrinkage after standing for 1 h at 150 °C. However, the Celgard separator has undergone significant thermal shrinkage as a result of its intrinsically low melting point. Therefore, considering the excellent mechanical
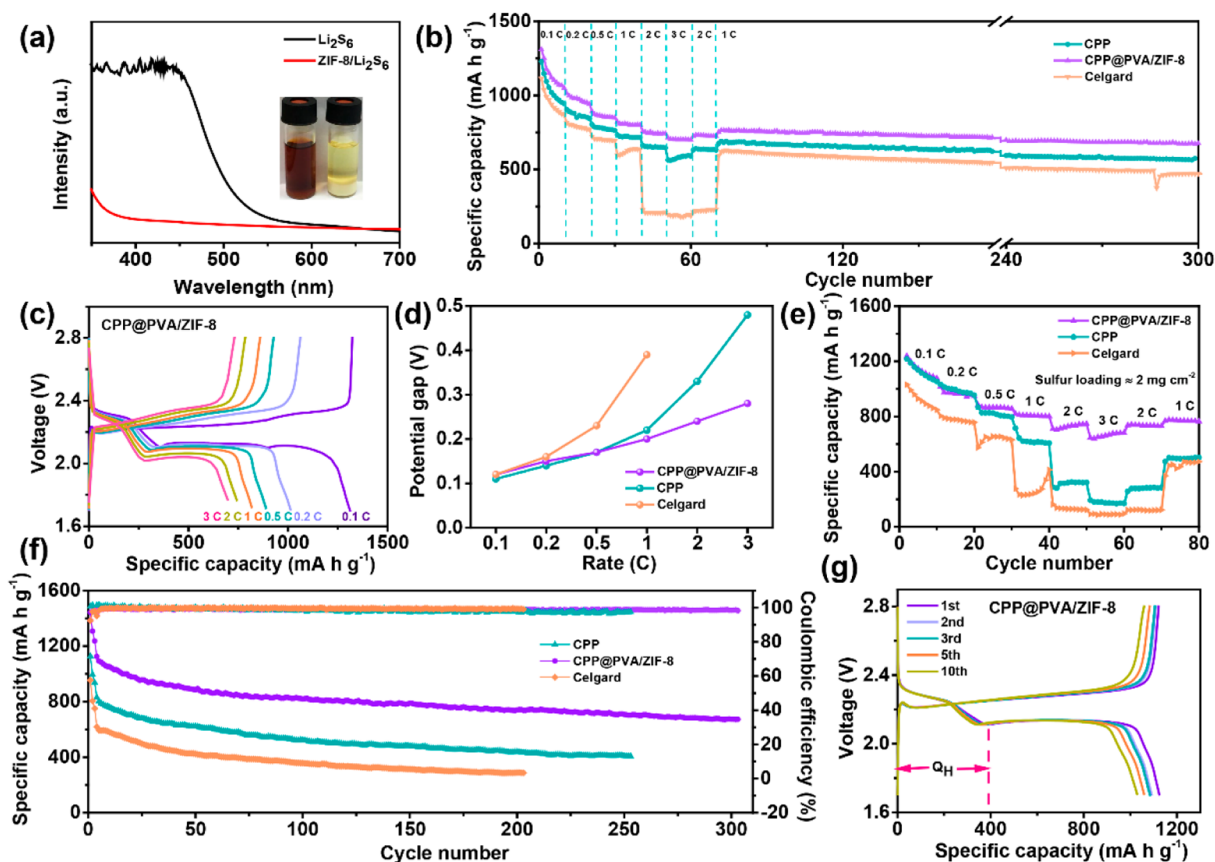
Figure 5. Electrochemical performance of Li−S cells with different separators: (a) UV−vis spectra, with the inset showing the corresponding photographs of pure LiPS solution and LiPS solution soaked with ZIF-8 particles, (b) rate capabilities of cells under 0.1−3 C and the long-term cycle performance at 1 C, (c) voltage profiles of the CPP@PVA/ZIF-8 separator at different current densities, (d) potential gap of cells with different separators at various rates, (e) rate capabilities with a high sulfur loading of 2 mg cm^{-2}, and (f) cycling performance with different separators at 0.2 C and (g) corresponding voltage profiles of CPP@PVA/ZIF-8 from first to tenth cycles.

stability, superior wettability, and thermal stability, the CPP@PVA/ZIF-8 separator is desired to provide excellent electrochemical stability for long-term LiPS immobilization and extend the cycle life of Li−S batteries.

According to the calculated ionic conductivities (Figure 4a and Figure S7 of the Supporting Information) and EIS results (Figure S8 of the Supporting Information), the commercial Celgard with inferior wettability displays a low Li$^+$ migration number (0.52) and ionic conductivity (0.019 mS cm^{-1}). In contrast, the superior wettability and 3D ionic transport channels profoundly improve the electrochemical dynamics of CPP@PVA/ZIF-8 and CPP nanofiber separators with large lithium transference numbers of 0.60 and 0.69 as well as high ionic conductivities of 0.037 and 0.04 mS cm^{-1}, respectively. The charge transfer resistance (R_{ct}) is also evaluated using the EIS test (Figure 4b). Clearly, the R_{ct} of the cell with a CPP separator has the smallest charge transfer resistance (19.3 Ω) as a result of the high ionic conductivity of the monolayer CPP separator. Although the bulk resistance (30.1 Ω) of the CPP@PVA/ZIF-8 separator is slightly higher than that of CPP for the larger charge transfer resistance after introduction of the PVA/ZIF-8 layer, it is still superior to that (43.2 Ω) of the bare Celgard separator. Considering the linear relationship between Z' and the square root of the frequency ($\omega_{0.5}$) in the low-frequency stage, the square of the slope in EIS is inversely proportional to the Li$^+$ diffusion coefficient (D_{Li^+}), which means that a small slope corresponds to a high Li$^+$ diffusion

rate. Therefore, the electrospun nanofiber-based CPP and CPP@PVA/ZIF-8 separators demonstrate faster Li$^+$ transfer efficiency with smaller slopes of 0.9 and 5.4 compared to that (5.8) of Celgard in Figure 4c.

To further obtain the electrochemical dynamics in relation to D_{Li^+}, CV tests are performed at different oxidation−reduction stages (Figure 4d). According to the Randles−Sevcik equation, the diffusion coefficient of the CPP@PVA/ZIF-8 separator is much higher than of Celgard (Figure 4e and Figure S9 and Table S3 of the Supporting Information), suggesting the superiority of the well-developed interconnected network of the CPP@PVA/ZIF-8 separator in facilitating efficient Li$^+$ transfer. The electrochemical stability of CPP@PVA/ZIF-8 is also explored through CV measurements at a sweep speed of 0.1 mV s^{-1}. As shown in Figure S10 of the Supporting Information, the two cathodic peaks around 2.25 and 2.05 V are ascribed to the transformation of the S$_8$ species to long-chain soluble LiPSs and the further reduction of LiPSs to insoluble Li$_2$S$_2$/Li$_2$S. In addition, the anodic peak around 2.4 V corresponds to the conversion of solid Li$_2$S$_2$/Li$_2$S to Li$_2$S$_8$/S through the multi-stage reactions. It can be well-observed that the redox peaks in the first to fifth cycles can perfectly overlap, manifesting that the cell assembled with the CPP@PVA/ZIF-8 separator possesses robust electrochemical reversibility. Therefore, the enhanced electrochemical kinetic and reversibility of the CPP@PVA/ZIF-8 separator, generated from the effective lithium ion transport in the highly developed interpenetrating
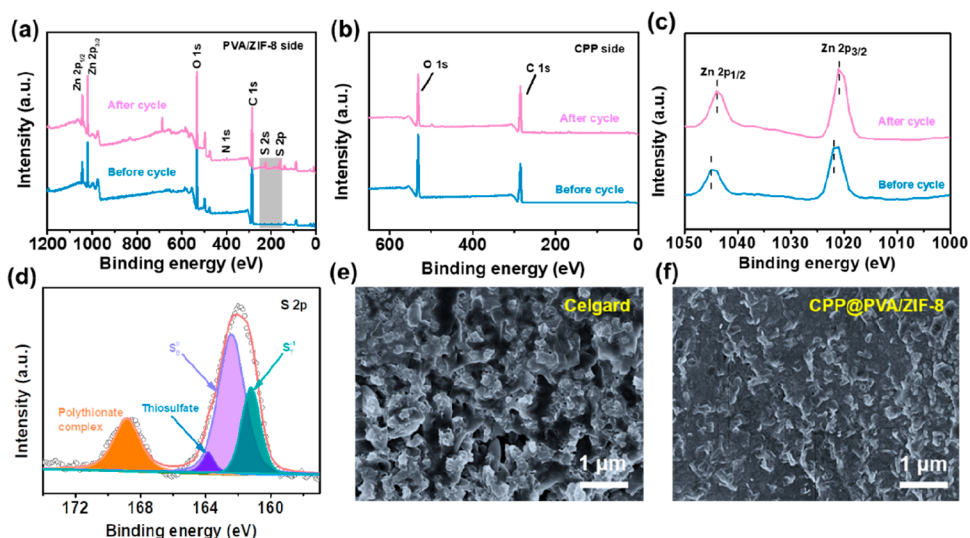
Figure 6. Surface chemistries of Li−S cells with the CPP@PVA/ZIF-8 separator before and after cycling: full-survey XPS spectra of the (a) PVA/ZIF-8 side and (b) CPP side for the CPP@PVA/ZIF-8 separator, high-resolution XPS spectra of (c) Zn 2p and (d) S 2s in the PVA/ZIF-8 side, and surface morphological changes of Li anodes after 100 cycles with (e) Celgard and (f) CPP@PVA/ZIF-8 separators.

nanofiber networks, is beneficial for the operation of the battery under long-term cycle.

Apart from the electrochemical dynamics, the practical LiPS immobilization ability of the fibrous separator is explored by the static absorption test. As shown in Figure 5a, the color of Li_2S_6 solution containing ZIF-8 turns faint yellow after standing for 1 h. Meanwhile, the ultraviolet−visible (UV−vis) absorption spectrum displays a significant decrease of the absorption peak at 350−450 nm, which is assigned to the $S_6^{2−}$ species, confirming the strong Lewis acid−base interactions and physical confinement between ZIF-8 and LiPSs.[30,49] Afterward, the rate performance is tested from 0.1 to 3 C, while the cycle performance is collected at 1 C for Celgard, CPP, and CPP@PVA/ZIF-8 separators. Both CPP and CPP@PVA/ZIF-8 separators exhibit higher reversible capacity than that of Celgard (Figure 5b). Despite the initial specific capacity of 1115.8 mAh g$^{−1}$ at 0.1 C, the Celgard separator delivers a severe deterioration in capacity from 596.7 to 209.1 mAh g$^{−1}$ caused by the shuttle of LiPSs under the high current density of 2 C. As for the CPP separator, the high initial discharge capacity of 1229.1 mAh g$^{−1}$ and stable cycle life are attributed to the enhanced electrochemical kinetics and efficient ionic shielding by the negatively charged carboxyl groups to LiPSs (Figure S11 of the Supporting Information). Notably, the cell with the CPP@PVA/ZIF-8 separator exhibits an excellent electrochemical reversibility with a high discharge capacity of 701.9 mAh g$^{−1}$, even at 3 C. When the current density returns to 1 C, a long-term cyclability with only 0.05% of the capacity decay rate is achieved for the CPP@PVA/ZIF-8 separator. This further proves the synergistic effects of effective electrostatic shielding from the electronegative CPP with numbers of COOH groups and physicochemical adsorption from ZIF-8 embedded on the cathode side of the fibrous CPP@PVA/ZIF-8 network. Galvanostatic charge/discharge profiles of different separators at various C rates are displayed in Figure 5c and Figure S12 of the Supporting Information. Benefiting from the high Li$^+$ transfer dynamics together with the strong LiPS immobilization on the cathode side of the asymmetric CPP@PVA/ZIF-8 separator, the corresponding cell displays the smallest polarization voltage at various C rates.

Figure 5d summarizes the polarization voltage at half of the discharge capacity for the first cycle. Obviously, the Celgard separator suffers from a sharp voltage rise, which is constrained by the low Li$^+$ migration efficiency and severe shuttle effect. In contrast, the electrostatic repulsion of the CPP separator toward LiPSs can partially alleviate the shuttle effect, thus achieving a lower potential gap. After incorporation of the anionic ZIF-8 nanoparticles in the CPP@PVA/ZIF-8 separator, a more stable rising trend is obtained. Therefore, the asymmetric design of the highly porous nanofiber membrane integrated with MOF-confined nanospaces can provide a fresh approach to achieve multiple immobilization of LiPSs as well as low polarization, excellent rate performance, and improved cycle stability of Li−S batteries.

High sulfur loading is another necessary aspect to evaluate the robust electrochemical performance for practical Li−S batteries. As illustrated in Figure 5e, the cell with the CPP@PVA/ZIF-8 separator with a high sulfur loading of 2 mg cm$^{−2}$ still delivers high reversible capacities of 1238.4, 1016.0, 882.9, 820.7, 710.1, and 646.4 mAh g$^{−1}$ at 0.1, 0.2, 0.5, 1, 2, and 3 C, respectively. Meanwhile, the long-term cyclability of the Li−S cells with different separators is investigated by activating at 0.05 C for the initial 3 cycles and continuously cycling at 0.2 C for 300 cycles (Figure 5f). Notably, the charge−discharge curves are well-overlapped from the first to tenth cycles in the Li−S cell with the CPP@PVA/ZIF-8 separator in Figure 5g. Being consistent with the CV curves, the first discharge plateau (Q_H) of CPP@PVA/ZIF-8, corresponding to the conversion of $S_8^{2−}$ to high-order Li_2S_x ($4 \leq x \leq 8$), reaches as high as 388 mAh g$^{−1}$ and remains at 229 mAh g$^{−1}$ after 300 cycles compared to those of CPP and Celgard separators (Figure S13 of the Supporting Information), confirming the good electrochemical stability of the CPP@PVA/ZIF-8 separator. Moreover, the cell with the CPP@PVA/ZIF-8 separator delivers an impressive long-term cycling stability with a very low capacity fading rate of 0.13% per cycle, which has proven to outperform most literature works (Table S4 of the Supporting Information).

To investigate the structural stability and LiPS shielding behavior of the nanofibrous CPP@PVA/ZIF-8 separator, a

practical Li−S cell is deconstructed after long cycling at 0.2 C. The SEM images display an original surface morphology without any deterioration in the asymmetric structure (panels a and b of Figure S14 of the Supporting Information), indicating the good electrochemical stability of the CPP@PVA/ZIF-8 separator for the effective inhibition of the shuttle effect during long-term redox environments. Besides, the corresponding elemental mapping of the PVA/ZIF-8 layer reveals that the Zn element is evenly distributed over the nanofiber network (Figure S14c of the Supporting Information). The ZIF-8 content in CPP@PVA/ZIF-8 is determined to be 15.3 wt % (Figure S14d of the Supporting Information), being consistent with its initial loading amount of 15.6 wt % in Figure S6 of the Supporting Information, further proving the firmly attached PVA/ZIF-8 network during the charge/discharge process. Meanwhile, the high-resolution XPS spectra are collected to understand the immobilization interactions between CPP@PVA/ZIF-8 and LiPSs. According to the full survey of the PVA/ZIF-8 side, the typical peaks of S 2s located at 226.0 eV and S 2p at 162.1 eV are clearly detected (Figure 6a). Nonetheless, the S element is absent in the CPP side (Figure 6b), which indicates that the dissolved LiPSs have been restricted to the cathode side by the strengthened adsorption between the PVA/ZIF-8 layer and LiPSs. After LiPSs are adsorbed by ZIF-8, a negative shift in the binding energy of Zn 2p can be observed (Figure 6c), suggesting that the exposed Zn sites with Lewis acidity can achieve an increased electron cloud density as a result of the chemical bonding between Zn and S to form a Lewis acid−base bond (Zn−S).[50,51] For the S 2p orbit in Figure 6d, the typical peaks at 161.2 and 162.4 eV are assigned to terminal S (S_T^{-1}) and bridging S (S_B^0) derived from freshly adsorbed polysulfides, respectively. Meanwhile, the characteristic peaks of S $2p_{3/2}$ at 163.8 and 168.9 eV are assigned to the thiosulfate and polysulfate compounds on the surface of the PVA/ZIF-8 layer.[50] All of these results show that the PVA/ZIF-8 functional layer can efficiently prevent the shuttling of LiPSs through strong chemical adsorption and physical confinement, while the CPP layer provides an electrostatic shielding to LiPSs. Hence, the SEM images present a much smoother lithium deposition surface with the protection of the CPP@PVA/ZIF-8 separator, while distinct cracks and porous Li dendrites are observed on the Li metal electrode assembled with the Celgard separator (panels e and f of Figure 6), which demonstrates the significant advantages of the anionic MOF-decorated fibrous separator in suppressing the polysulfide shuttle for potential applications in high-performance Li−S batteries.

4. CONCLUSION

In summary, a newly modified separator of a MOF-decorated polymer nanofiber separator with a Janus structure has been demonstrated on the basis of the electrostatic shielding and chemical adsorption mechanisms. Through the facile electro-spinning and electrospray coupling procedure, the integrated nanofibrous separator not only exhibits remarkable wettability and thermostability but also expedites the ion transport upon cycling. Furthermore, the small pore size and chemisorption features of PVA/ZIF-8 can physicochemically block LiPS shuttling, while the negatively charged fibrous CPP layer ensures the efficient ionic shielding toward LiPSs. Benefiting from the synergetic advantages, the Li−S cell assembled with the CPP@PVA/ZIF-8 separator delivers a significantly improved rate capability with a slow capacity attenuation of

0.05% per cycle and a long cycling performance at 0.1 C. We believe that the functional MOF-integrated electrospun nanofiber membrane with unique architectures may provide a novel route for the design of advanced Li−S separators.

■ ASSOCIATED CONTENT

Ⓢ Supporting Information

The Supporting Information is available free of charge at https://pubs.acs.org/doi/10.1021/acs.energyfuels.1c02081.

> SEM and TEM images, TGA curves, pore size distributions, electrolyte wettability, mechanical properties, electrochemical performance of different separators, and tables for the respective physical properties and Li$^+$ diffusion coefficient (PDF)

■ AUTHOR INFORMATION

Corresponding Authors

Yue-E Miao − *State Key Laboratory for Modification of Chemical Fibers and Polymer Materials, College of Materials Science and Engineering, Donghua University, Shanghai 201620, People's Republic of China;* ⓘ orcid.org/0000-0002-3660-029X; Email: yuee_miao@dhu.edu.cn

Yi Xie − *Hefei National Laboratory for Physical Sciences at the Microscale, CAS Centre for Excellence in Nanoscience, iCHEM, University of Science and Technology of China, Hefei, Anhui 230026, People's Republic of China;* ⓘ orcid.org/0000-0002-1416-5557; Email: yxie@ustc.edu.cn

Authors

Shujun Zheng − *State Key Laboratory for Modification of Chemical Fibers and Polymer Materials, College of Materials Science and Engineering, Donghua University, Shanghai 201620, People's Republic of China*

Xiaobo Zhu − *State Key Laboratory for Modification of Chemical Fibers and Polymer Materials, College of Materials Science and Engineering, Donghua University, Shanghai 201620, People's Republic of China*

Yue Ouyang − *State Key Laboratory for Modification of Chemical Fibers and Polymer Materials, College of Materials Science and Engineering, Donghua University, Shanghai 201620, People's Republic of China*

Kai Chen − *State Key Laboratory for Modification of Chemical Fibers and Polymer Materials, College of Materials Science and Engineering, Donghua University, Shanghai 201620, People's Republic of China*

Ai-Long Chen − *State Key Laboratory for Modification of Chemical Fibers and Polymer Materials, College of Materials Science and Engineering, Donghua University, Shanghai 201620, People's Republic of China*

Xiaoshan Fan − *State Key Laboratory for Modification of Chemical Fibers and Polymer Materials, College of Materials Science and Engineering, Donghua University, Shanghai 201620, People's Republic of China;* ⓘ orcid.org/0000-0002-0617-7400

Tianxi Liu − *State Key Laboratory for Modification of Chemical Fibers and Polymer Materials, College of Materials Science and Engineering, Donghua University, Shanghai 201620, People's Republic of China; Key Laboratory of Synthetic and Biological Colloids, Ministry of Education, School of Chemical and Material Engineering, Jiangnan University, Wuxi, Jiangsu 214122, People's Republic of China*

Complete contact information is available at:
https://pubs.acs.org/10.1021/acs.energyfuels.1c02081

■ REFERENCES

(1) Zhou, G.; Yang, A.; Gao, G.; Yu, X.; Xu, J.; Liu, C.; Ye, Y.; Pei, A.; Wu, Y.; Peng, Y.; Li, Y.; Liang, Z.; Liu, K.; Wang, L. W.; Cui, Y. Supercooled Liquid Sulfur Maintained in Three-Dimensional Current Collector for High-Performance Li-S Batteries. *Sci. Adv.* **2020**, *6* (21), No. eaay5098.

(2) Pang, Q.; Kundu, D.; Cuisinier, M.; Nazar, L. F. Surface-Enhanced Redox Chemistry of Polysulphides on a Metallic and Polar Host for Lithium-Sulphur Batteries. *Nat. Commun.* **2014**, *5* (1), 4759.

(3) Li, B.-Q.; Kong, L.; Zhao, C.-X.; Jin, Q.; Chen, X.; Peng, H.-J.; Qin, J.-L.; Chen, J.-X.; Yuan, H.; Zhang, Q.; Huang, J. Q. Expediting Redox Kinetics of Sulfur Species by Atomic-Scale Electrocatalysts in Lithium—Sulfur Batteries. *InfoMat.* **2019**, *1* (4), 533—541.

(4) Shaibani, M.; Mirshekarloo, M. S.; Singh, R.; Easton, C. D.; Cooray, M. C. D.; Eshraghi, N.; Abendroth, T.; Dörfler, S.; Althues, H.; Kaskel, S.; Hollenkamp, A. F.; Hill, M. R.; Majumder, M. Expansion-Tolerant Architectures for Stable Cycling of Ultrahigh-Loading Sulfur Cathodes in Lithium-Sulfur Batteries. *Sci. Adv.* **2020**, *6* (1), No. eaay2757.

(5) Su, D.; Zhou, D.; Wang, C.; Wang, G. Toward High Performance Lithium—Sulfur Batteries Based on Li_2S Cathodes and Beyond: Status, Challenges, and Perspectives. *Adv. Funct. Mater.* **2018**, *28* (38), 1800154.

(6) Whittingham, M. S. Lithium Batteries and Cathode Materials. *Chem. Rev.* **2004**, *104* (10), 4271—4302.

(7) Lin, D.; Liu, Y.; Cui, Y. Reviving the Lithium Metal Anode for High-Energy Batteries. *Nat. Nanotechnol.* **2017**, *12* (3), 194—206.

(8) Yu, X.; Joseph, J.; Manthiram, A. Suppression of the Polysulfide-Shuttle Behavior in Li—S Batteries through the Development of a Facile Functional Group on the Polypropylene Separator. *Mater. Horiz.* **2016**, *3* (4), 314—319.

(9) Li, G.; Wang, S.; Zhang, Y.; Li, M.; Chen, Z.; Lu, J. Revisiting the Role of Polysulfides in Lithium—Sulfur Batteries. *Adv. Mater.* **2018**, *30* (22), 1705590.

(10) Chen, Y.; Zhou, G.; Zong, W.; Ouyang, Y.; Chen, K.; Lv, Y.; Miao, Y.-E.; Liu, T. Porous Polymer Composite Separators with Three-Dimensional Ion-Selective Nanochannels for High-Performance Li—S Batteries. *Compos. Commun.* **2021**, *25*, 100679.

(11) Bhargav, A.; He, J.; Gupta, A.; Manthiram, A. Lithium-Sulfur Batteries: Attaining the Critical Metrics. *Joule* **2020**, *4* (2), 285—291.

(12) Wang, X.; Yang, C.; Xiong, X.; Chen, G.; Huang, M.; Wang, J.-H.; Liu, Y.; Liu, M.; Huang, K. A Robust Sulfur Host with Dual Lithium Polysulfide Immobilization Mechanism for Long Cycle Life and High Capacity Li-S Batteries. *Energy Storage Mater.* **2019**, *16*, 344—353.

(13) Li, J.; Wei, W.; Meng, L. Liquid-Phase Exfoliated-Graphene-Supporting Nanostructural Sulfur as High-Performance Lithium—Sulfur Batteries Cathode. *Compos. Commun.* **2019**, *15*, 149—154.

(14) Li, Z.; Zhang, J.; Lou, X. W. Hollow Carbon Nanofibers Filled with MnO_2 Nanosheets as Efficient Sulfur Hosts for Lithium—Sulfur Batteries. *Angew. Chem., Int. Ed.* **2015**, *54* (44), 12886—12890.

(15) Liang, X.; Kwok, C. Y.; Lodi-Marzano, F.; Pang, Q.; Cuisinier, M.; Huang, H.; Hart, C. J.; Houtarde, D.; Kaup, K.; Sommer, H.;

Brezesinski, T.; Janek, J.; Nazar, L. F. Tuning Transition Metal Oxide—Sulfur Interactions for Long Life Lithium Sulfur Batteries: The "Goldilocks" Principle. *Adv. Energy Mater.* **2016**, *6* (6), 1501636.

(16) Zeng, Z.; Li, W.; Chen, X.; Zhang, N.; Qi, H.; Liu, X. Nanosized FeS_2 Particles Caged in the Hollow Carbon Shell as a Robust Polysulfide Adsorbent and Redox Mediator. *ACS Sustainable Chem. Eng.* **2020**, *8* (8), 3261—3272.

(17) Zhou, W.; Wang, C.; Zhang, Q.; Abruña, H. D.; He, Y.; Wang, J.; Mao, S. X.; Xiao, X. Tailoring Pore Size of Nitrogen-Doped Hollow Carbon Nanospheres for Confining Sulfur in Lithium—Sulfur Batteries. *Adv. Energy Mater.* **2015**, *5* (16), 1401752.

(18) Ma, C.; Feng, Y.; Liu, X.; Yang, Y.; Zhou, L.; Chen, L.; Yan, C.; Wei, W. Dual-Engineered Separator for Highly Robust, All-Climate Lithium-Sulfur Batteries. *Energy Storage Mater.* **2020**, *32*, 46—54.

(19) Chen, X.; Zhang, R.; Zhao, R.; Qi, X.; Li, K.; Sun, Q.; Ma, M.; Qie, L.; Huang, Y. A "Dendrite-Eating" Separator for High-Areal-Capacity Lithium-Metal Batteries. *Energy Storage Mater.* **2020**, *31*, 181—186.

(20) Dai, J.; Shi, C.; Li, C.; Shen, X.; Peng, L.; Wu, D.; Sun, D.; Zhang, P.; Zhao, J. A Rational Design of Separator with Substantially Enhanced Thermal Features for Lithium-Ion Batteries by the Polydopamine—Ceramic Composite Modification of Polyolefin Membranes. *Energy Environ. Sci.* **2016**, *9* (10), 3252—3261.

(21) Lei, T.; Chen, W.; Hu, Y.; Lv, W.; Lv, X.; Yan, Y.; Huang, J.; Jiao, Y.; Chu, J.; Yan, C.; Wu, C.; Li, Q.; He, W.; Xiong, J. A Nonflammable and Thermotolerant Separator Suppresses Polysulfide Dissolution for Safe and Long-Cycle Lithium-Sulfur Batteries. *Adv. Energy Mater.* **2018**, *8* (32), 1802441.

(22) Huang, X.; He, R.; Li, M.; Chee, M. O. L.; Dong, P.; Lu, J. Functionalized Separator for Next-Generation Batteries. *Mater. Today* **2020**, *41*, 143—155.

(23) Tong, Z.; Huang, L.; Liu, H.; Lei, W.; Zhang, H.; Zhang, S.; Jia, Q. Defective Graphitic Carbon Nitride Modified Separators with Efficient Polysulfide Traps and Catalytic Sites for Fast and Reliable Sulfur Electrochemistry. *Adv. Funct. Mater.* **2021**, *31* (11), 2010455.

(24) Yin, L.; Wang, J.; Lin, F.; Yang, J.; Nuli, Y. Polyacrylonitrile/Graphene Composite as a Precursor to a Sulfur-Based Cathode Material for High-Rate Rechargeable Li—S Batteries. *Energy Environ. Sci.* **2012**, *5* (5), 6966—6972.

(25) Li, W.; Zhang, Q.; Zheng, G.; Seh, Z. W.; Yao, H.; Cui, Y. Understanding the Role of Different Conductive Polymers in Improving the Nanostructured Sulfur Cathode Performance. *Nano Lett.* **2013**, *13* (11), 5534—5540.

(26) Zuo, X.; Zhen, M.; Wang, C. Ni@N-Doped Graphene Nanosheets and CNTs Hybrids Modified Separator as Efficient Polysulfide Barrier for High-Performance Lithium Sulfur Batteries. *Nano Res.* **2019**, *12* (4), 829—836.

(27) Ma, C.; Zhang, Y. Q.; Feng, Y. M.; Wang, N.; Zhou, L. J.; Liang, C. P.; Chen, L. B.; Lai, Y. Q.; Ji, X. B.; Yan, C. L.; Wei, W. F. Engineering Fe—N Coordination Structures for Fast Redox Conversion in Lithium—Sulfur Batteries. *Adv. Mater.* **2021**, *33*, 2100171.

(28) Wu, X.; Fan, L.; Qiu, Y.; Wang, M.; Cheng, J.; Guan, B.; Guo, Z.; Zhang, N.; Sun, K. Ion-Selective Prussian-Blue-Modified Celgard Separator for High-Performance Lithium-Sulfur Battery. *ChemSusChem* **2018**, *11* (18), 3345—3351.

(29) Bai, S.; Liu, X.; Zhu, K.; Wu, S.; Zhou, H. Metal—Organic Framework-Based Separator for Lithium—Sulfur Batteries. *Nat. Energy* **2016**, *1* (7), 16094.

(30) Chiochan, P.; Yu, X.; Sawangphruk, M.; Manthiram, A. A Metal Organic Framework Derived Solid Electrolyte for Lithium—Sulfur Batteries. *Adv. Energy Mater.* **2020**, *10* (27), 2001285.

(31) Zheng, Z. J.; Ye, H.; Guo, Z. P. Recent Progress on Pristine Metal/Covalent-Organic Frameworks and Their Composites for Lithium—Sulfur Batteries. *Energy Environ. Sci.* **2021**, *14* (4), 1835—1853.

(32) Zhang, X.; Li, G.; Zhang, Y.; Luo, D.; Yu, A.; Wang, X.; Chen, Z. Amorphizing Metal-Organic Framework towards Multifunctional

Polysulfide Barrier for High-Performance Lithium-Sulfur Batteries. *Nano Energy* **2021**, *86*, 106094.

(33) Gao, G. K.; Wang, Y. R.; Wang, S. B.; Yang, R. X.; Chen, Y.; Zhang, Y.; Jiang, C.; Wei, M. J.; Ma, H.; Lan, Y. Q. Stepped Channels Integrated Lithium−Sulfur Separator via Photoinduced Multidimensional Fabrication of Metal−Organic Frameworks. *Angew. Chem., Int. Ed.* **2021**, *60* (18), 10147−10154.

(34) Wang, Z.; Huang, W.; Hua, J.; Wang, Y.; Yi, H.; Zhao, W.; Zhao, Q.; Jia, H.; Fei, B.; Pan, F. An Anionic-MOF-Based Bifunctional Separator for Regulating Lithium Deposition and Suppressing Polysulfides Shuttle in Li−S Batteries. *Small Methods* **2020**, *4* (7), 2000082.

(35) Bai, S.; Kim, B.; Kim, C.; Tamwattana, O.; Park, H.; Kim, J.; Lee, D.; Kang, K. Permselective Metal−Organic Framework Gel Membrane Enables Long-Life Cycling of Rechargeable Organic Batteries. *Nat. Nanotechnol.* **2021**, *16* (1), 77−84.

(36) Zhou, C. Y.; Wang, J.; Zhu, X. B.; Chen, K.; Ouyang, Y.; Wu, Y.; Miao, Y. E.; Liu, T. X. A Dual-Functional Poly(Vinyl Alcohol)/Poly(Lithium Acrylate) Composite Nanofiber Separator for Ionic Shielding of Polysulfides Enables High-Rate and Ultra-Stable Li-S Batteries. *Nano Res.* **2021**, *14*, 1541−1550.

(37) Sun, Z.; Xiao, M.; Wang, S.; Han, D.; Song, S.; Chen, G.; Meng, Y. Electrostatic Shield Effect: An Effective Way to Suppress Dissolution of Polysulfide Anions in Lithium−Sulfur Battery. *J. Mater. Chem. A* **2014**, *2* (38), 15938−15944.

(38) Zhang, C.; Shen, L.; Shen, J.; Liu, F.; Chen, G.; Tao, R.; Ma, S.; Peng, Y.; Lu, Y. Anion-Sorbent Composite Separators for High-Rate Lithium-Ion Batteries. *Adv. Mater.* **2019**, *31* (21), 1808338.

(39) Hu, G.; Zhang, X.; Liu, X.; Yu, J.; Ding, B. Electrospun Nanofibers Withstandable to High-Temperature Reactions: Synergistic Effect of Polymer Relaxation and Solvent Removal. *Adv. Fiber Mater.* **2021**, *3* (1), 14−25.

(40) Li, Y.; Shen, Q.; Shen, J.; Ding, X.; Liu, T.; He, J.; Zhu, C.; Zhao, D.; Zhu, J. Multifunctional Fibroblasts Enhanced via Thermal and Freeze-Drying Post-Treatments of Aligned Electrospun Nanofiber Membranes. *Adv. Fiber Mater.* **2021**, *3* (1), 26−37.

(41) Dwyer, D. B.; E. Mera, E.; Gudavalli, G. S.; Bernier, W. E.; Dhakal, T. P.; Jones, W. E. Homogeneous Titanium Hydroxide Yields Hydroxyl Decorated Nanofiber Separator with Improved Electrolyte Uptake and Device Capacitance. *Mater. Lett.* **2021**, *284*, 129023.

(42) Liu, H.; Li, C.; Zhang, H. P.; Fu, L. J.; Wu, Y. P.; Wu, H. Q. Kinetic Study on LiFePO$_4$/C Nanocomposites Synthesized by Solid State Technique. *J. Power Sources* **2006**, *159* (1), 717−720.

(43) Huang, J. Q.; Zhuang, T. Z.; Zhang, Q.; Peng, H. J.; Chen, C. M.; Wei, F. Permselective Graphene Oxide Membrane for Highly Stable and Anti-Self-Discharge Lithium−Sulfur Batteries. *ACS Nano* **2015**, *9* (3), 3002−3011.

(44) Zhou, L.; Li, N.; Owens, G.; Chen, Z. Simultaneous Removal of Mixed Contaminants, Copper and Norfloxacin, from Aqueous Solution by ZIF-8. *Chem. Eng. J.* **2019**, *362*, 628−637.

(45) Jia, Z.; Wu, G.; Wu, D.; Tong, Z.; Winston Ho, W. S. Preparation of Ultra-Stable ZIF-8 Dispersions in Water and Ethanol. *J. Porous Mater.* **2017**, *24* (6), 1655−1660.

(46) Sun, C.; Zhang, J.; Yuan, X.; Duan, J.; Deng, S.; Fan, J.; Chang, J.-K.; Zheng, M.; Dong, Q. ZIF-8-Based Quasi-Solid-State Electrolyte for Lithium Batteries. *ACS Appl. Mater. Interfaces* **2019**, *11* (50), 46671−46677.

(47) Pieczonka, N. P. W.; Borgel, V.; Ziv, B.; Leifer, N.; Dargel, V.; Aurbach, D.; Kim, J. H.; Liu, Z.; Huang, X.; Krachkovskiy, S. A.; Goward, G. R.; Halalay, I.; Powell, B. R.; Manthiram, A. Lithium Polyacrylate (LiPAA) as an Advanced Binder and a Passivating Agent for High-Voltage Li-Ion Batteries. *Adv. Energy Mater.* **2015**, *5* (23), 1501008.

(48) Su, A.; Pang, Q.; Chen, X.; Dong, J.; Zhao, Y.; Lian, R.; Zhang, D.; Liu, B.; Chen, G.; Wei, Y. Lithium Poly-Acrylic Acid as a Fast Li$^+$ Transport Media and a Highly Stable Aqueous Binder for Li$_3$V$_2$(PO$_4$)$_3$ Cathode Electrodes. *J. Mater. Chem. A* **2018**, *6* (46), 23357−23365.

(49) Wu, Z. S.; Parvez, K.; Winter, A.; Vieker, H.; Liu, X.; Han, S.; Turchanin, A.; Feng, X.; Müllen, K. Layer-by-Layer Assembled Heteroatom-Doped Graphene Films with Ultrahigh Volumetric Capacitance and Rate Capability for Micro-Supercapacitors. *Adv. Mater.* **2014**, *26* (26), 4552−4558.

(50) Wu, F.; Zhao, S.; Chen, L.; Lu, Y.; Su, Y.; Jia, Y.; Bao, L.; Wang, J.; Chen, S.; Chen, R. Metal-Organic Frameworks Composites Threaded on the CNT Knitted Separator for Suppressing the Shuttle Effect of Lithium Sulfur Batteries. *Energy Storage Mater.* **2018**, *14*, 383−391.

(51) Li, G.; Lei, W.; Luo, D.; Deng, Y.; Deng, Z.; Wang, D.; Yu, A.; Chen, Z. Stringed "Tube on Cube" Nanohybrids as Compact Cathode Matrix for High-Loading and Lean-Electrolyte Lithium−Sulfur Batteries. *Energy Environ. Sci.* **2018**, *11* (9), 2372−2381.